Geothermics 76 (2018) 231–241

Contents lists available at ScienceDirect

Geothermics

journal homepage: www.elsevier.com/locate/geothermics

Understanding amorphous silica scaling under well-constrained conditions inside geothermal pipelines

Daniela B. van den Heuvel[a,*], Einar Gunnlaugsson[b], Ingvi Gunnarsson[b], Tomasz M. Stawski[a,c], Caroline L. Peacock[a], Liane G. Benning[a,c,d]

[a] Cohen Geochemistry Group, School of Earth and Environment, University of Leeds, Leeds, LS2 9JT, UK
[b] Reykjavik Energy, Bæjarhals 1, 110, Reykjavik, Iceland
[c] German Research Center for Geosciences, GFZ, 14473, Potsdam, Germany
[d] Department of Earth Sciences, Free University of Berlin, 12249, Berlin, Germany

ARTICLE INFO

Keywords:
Silica
Geothermal energy
Precipitation
Mineral scaling
Silica sinter

ABSTRACT

Amorphous silica is a common precipitate in modern and ancient hot springs and in geothermal power plants, yet the corresponding precipitation rates and mechanisms are still highly debated, primarily due to the plethora of parameters that can affect the reactions in natural waters. Here, we report the results from a first ever industrial-scale time-resolved (1 day to 10 weeks) study of silica precipitation conducted at the Hellisheiði geothermal power plant (SW-Iceland). We show that such in-work pipelines of a geothermal power plant are ideal environments to investigate silica precipitation because the physicochemical conditions are well constrained and constantly monitored. Our results document that amorphous silica forms via two distinct precipitation modes: (1) the fast deposition of continuous botryoidal silica layers and (2) the growth of 3D fan- or ridge-shaped silica aggregates. The continuous layers grow by heterogeneous nucleation and subsequent surface controlled growth by monomer addition. In contrary, the 3D aggregates form through homogeneous nucleation of silica nano- and microparticles in solution, followed by deposition and cementation on the surface of the botryoidal layer. From the time-resolved data, silica precipitation rates of over 1 g m^{-2} day^{-1} are derived. Over time, this deposition of silica on pipelines and fluid handling equipment is detrimental to geothermal power production. Our data does not only help improve our understanding of silica precipitation from geothermal fluids, but the determined silica precipitation mechanisms and rates help improve mitigation strategies against silica scaling inside in-work geothermal power plants.

1. Introduction

Silica (SiO_2) is the most common chemical compound in the Earth's crust and a major component in most geothermal reservoirs. The maximum concentration of silica in geothermal fluids depends on the reservoir temperature and is controlled by quartz solubility or, if the temperature is below 110 °C, by the solubility of chalcedony (Arnórsson, 1975; Fournier and Rowe, 1966). When these geothermal fluids rise through the crust and emerge at the Earth's surface, rapid cooling results in supersaturation with respect to amorphous silica and precipitation. This sinter formation was studied in numerous modern and ancient terrestrial settings (Braunstein and Lowe, 2001; Cady and Farmer, 1996; Handley et al., 2005; Jones and Renaut, 2004; Konhauser et al., 2004, 2001; Mountain et al., 2003; Tobler et al., 2008) and recently, evidence for ancient silica sinter formation has even been documented on Mars (Preston et al., 2008).

Identical to their natural analogues, amorphous silica precipitation also occurs in geothermal power plants, where fluids are rapidly cooled during energy production, resulting in precipitation of amorphous silica. This so called "silica scaling" is common in high-enthalpy geothermal power plants around the world e.g. Iceland, New Zealand, Japan, the USA, the Lesser Antilles and El Salvador (Dixit et al., 2016; Gunnarsson and Arnórsson, 2003, 2005; Harrar et al., 1982; Meier et al., 2014; Mroczek et al., 2017; Padilla et al., 2005; Rothbaum et al., 1979; Yokoyama et al., 1993). In such systems, amorphous silica precipitation occurs in fluids characterized by a wide range of total silica concentrations (250–900 mg/L), temperatures (20–200 °C), pH (7.2–10.2), total dissolved solid concentrations (1300–93′000 mg/L) and different types of geothermal power plants (e.g. flash steam and binary). Because of the ubiquity and importance of this natural process

* Corresponding author. Current address: Rock-Water Interaction Group, Institute of Geological Sciences, University of Bern, 3012, Bern, Switzerland.
E-mail address: daniela.vandenheuvel@geo.unibe.ch (D.B. van den Heuvel).

https://doi.org/10.1016/j.geothermics.2018.07.006
Received 30 November 2017; Received in revised form 23 April 2018; Accepted 5 July 2018
Available online 07 August 2018
0375-6505/

to renewable energy production and sinter formation, amorphous silica precipitation was studied extensively in the laboratory. Amorphous silica forms via the condensation of silica monomers (H_4SiO_4) into Si-O-Si bonds (Iler, 1979), through polymerisation that can either occur at an interface (e.g., minerals, bacteria or plant matter) where it is described as "heterogeneous nucleation" or in the bulk fluid ("homogeneous nucleation") (Benning and Waychunas, 2007). In both cases, once silica nuclei have reached a critical size (< 0.5 to 2 nm, Iler, 1979; Noguera et al., 2015; Tobler et al., 2009), they grow spontaneously by the addition of silica from solution. Monomers are the dominant growth species (Bohlmann et al., 1976; Bremere et al., 2000; Mroczek and McDowell, 1988) due to their predominantly neutral charge ($K_a \sim 10^{-8.8}$ at 120 °C) (Fleming and Crerar, 1982; Seward, 1974) in the slightly alkaline pH regime of silica-rich geothermal waters. In contrast, silica polymers and nuclei have a higher dissociation constant ($K_a > 10^{-8}$) (Dugger et al., 1964; Hair and Hertl, 1970), resulting in an overall negative surface charge. Their attachment to existing silica particles or surfaces and the aggregation of silica particles in solution in the absence of bridging cations will thus be limited by electrostatic repulsion. Experimental evidence showed that silica polymerisation, nucleation and growth are enhanced at slightly alkaline pH, elevated temperature, medium to high ionic strength (especially the presence of Al and Fe) and high total silica concentrations (Alexander et al., 1954; Crerar et al., 1981; Fleming, 1986; Gallup, 1997; Goto, 1956; Gunnarsson and Arnórsson, 2005; Icopini et al., 2005; Iler, 1979; Kitahara, 1960; Tobler and Benning, 2013; Weres et al., 1981).

These physicochemical factors also affect amorphous silica precipitation from naturally occurring geothermal fluids, where they are in competition with one another and it is often difficult to isolate the dominant parameter in any given fluid. In addition, microbial activity in hot springs (Mountain et al., 2003; Tobler et al., 2008) and high flow rates in geothermal power plants (Meier et al., 2014) make the understanding of these systems highly challenging. Therefore, most laboratory findings cannot be directly transferred and applied to silica precipitation from natural geothermal fluids (Carroll et al., 1998) and although a number of field studies investigating silica sinter formation around hot springs (e.g. Braunstein and Lowe, 2001; Handley et al., 2005; Jones and Renaut, 2004; Konhauser et al., 2004; Mountain et al., 2003; Tobler et al., 2008) give insights into what happens once geothermal solutions reach the Earth surface, they do not address processes that govern formation of amorphous silica inside geothermal power plants. This is despite the fact that in-production geothermal power plants represent systems with very well constrained physicochemical conditions that are thus ideal sites to investigate silica precipitation. Such studies would not just help quantify real world silica precipitation but would also inform silica scaling mitigation strategies, thus improving efficiency of geothermal energy production and reduce costs.

The main reason for the dearth of on-site studies lies in the difficulties in accessing both fluids and silica scales during energy production, without affecting normal operations. A few studies aimed to circumvent these problems by conducting experiments in bypass systems from the main production (Carroll et al., 1998; Dixit et al., 2016; Harrar et al., 1982; Mroczek et al., 2017; Rothbaum et al., 1979). However, the conditions in such bypass systems are most often markedly different from inside in-work pipelines and the bypass is often less well constrained, resulting in data that are only partly applicable to the in-production systems.

To change this landscape, we have for the first time conducted a detailed study inside actual in-work geothermal pipelines of a high enthalpy geothermal power plant at Hellisheiði, SW-Iceland. We monitored silica precipitation for up to 10 weeks using stainless steel scaling plates deployed at different positions within the pipelines and characterized the precipitated solids, as well as fluid composition and the physicochemical conditions, under which precipitation occurred. Our results reveal that two largely independent pathways control silica precipitation. We observe the formation of a continuous, botryoidal layer of silica on the scaling plate surfaces and the growth of 3D structures consisting of silica particles that nucleate homogeneously in the fast travelling fluid and are then deposited and cemented to the silica layer. Through this work, we evaluate the first ever amorphous silica precipitation rates and mechanisms inside in operando pipelines of an active geothermal power plant.

Table 1
Duration and starting/end dates of individual scaling plate deployments. The cleaning of the heat exchangers in early October 2014 (after the 10 week and before the 2 week deployment) was part of regular (every 4–6 months) and scheduled maintenance at the Hellisheiði power plant to remove the accumulated silica scales.

	Deployment [days]	Start date	End date
1 day	1	02/02/2015	03/02/2015
3 days	3	16/03/2015	19/03/2015
1 week	7	27/10/2014	03/11/2014
2 weeks	14	03/11/2014	17/11/2014
4 weeks	28	23/06/2014	21/07/2014
6 weeks	41	03/02/2015	16/03/2015
10 weeks	72	21/07/2014	01/10/2014
Cleaning of heat exchangers		06/10/2014	07/10/2014

2. Materials and methods

2.1. Field deployments

The time-resolved deposition of amorphous silica was studied on stainless steel scaling plates (5.4 × 2–2.5 cm) deployed for between 1 day and 10 weeks (Table 1) at four different locations within the pipelines of the Hellisheiði power plant (Fig. 1): (1) several metres before the heat exchangers, (2) several metres after the heat exchangers, (3) several tens of metres downstream of location 2, after a bypass with fluid that had not passed through the heat exchangers that then rejoined the main pipeline and before mixing with condensed steam (equivalent to almost pure water) and (4) ~1300 m downstream from location 3, at the Húsmúli re-injection site. These locations were chosen because they differed with respect to physicochemical conditions of the fluid (temperature, flow rate, silica concentration etc.) thus allowing us to study how these parameters affected silica precipitation. It is worth noting that due to operational constraints the time resolved deployments were not done in order of deployment length (Table 1).

At each location, scaling plates made from S316 stainless steel (Fig. 1B–D) were attached to a sampling rod and inserted into the fast flowing geothermal fluid through valves in the pipeline walls. The surfaces of the plates were aligned to be parallel to the flow. The power plant operators monitor the temperatures and flow rates at each of the chosen sampling locations hourly to identify changes in production parameters and as a guide for when maintenance (e.g., heat exchanger cleaning) is required. These continuous datasets helped make sure that the scaling plate deployments were started/finished during periods where no maintenance was required. At the end of each deployment, the plates were removed from the fluid, gently rinsed with distilled water to prevent the precipitation of salts during evaporation of the geothermal fluid and then dried at 40 °C for up to 16 h. For short deployments (1 day, 3 days and 1 week), the scaling plates were weighted pre- and post-deployment in order to determine the mass of precipitated silica. For deployments of 2 weeks or longer this was not considered feasible as in most cases larger amounts of silica precipitated on the plates and some of the accumulated silica would have been either lost because of the fast fluid flow rates (fluid flow 280 to 430 L/s) or during scaling plate handling post removal.

At the beginning and end of each deployment, the fluid at each location was sampled. It was cooled down to ambient values (21–27 °C) using a ~5 m stainless steel coil and temperature and pH were

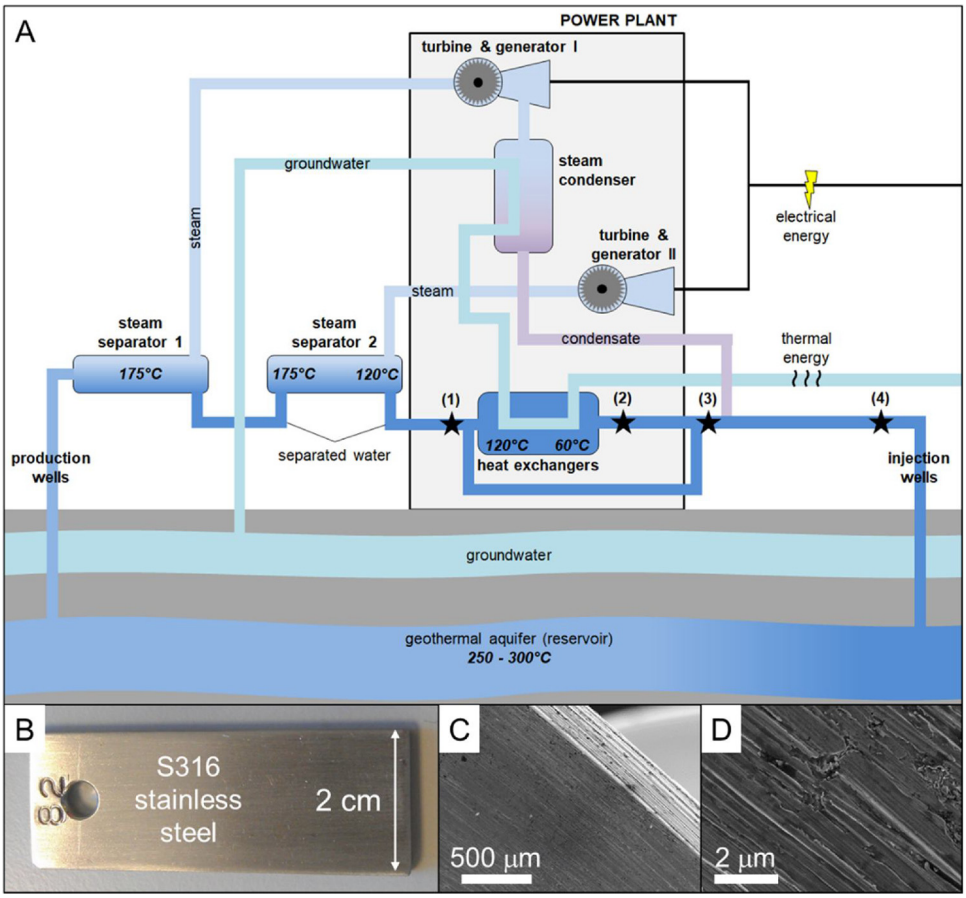

Fig. 1. System schematic of the Hellisheiði geothermal power plant (A) indicating the four sampling locations (stars) at which the scaling plates (B) were immersed. FEG-SEM images (C & D) showing the irregular texture of the steel surfaces before deployment.

measured using a Metrohm Aquatrode plus pH electrode with a thermocouple. Fluid samples were then collected into two Teflon gas sampling bulbs (300 mL, rinsed 3x with separated water before use), assuring no air remained trapped within the bulbs. These samples were used for analysis of dissolved CO_2 and H_2S. Subsequently a stainless steel holder containing single-use 0.2 µm polycarbonate filter membranes (Whatman®) was used to collect filtered fluid samples. These samples were divided into three different aliquots. For cation analyses, aliquots were transferred into 120 mL into Nalgene bottles containing 2.5 mL of ultrapure HNO_3 while for anions, 60 mL of the filtered geothermal fluid were transferred into pre-cleaned Nalgene bottles. At selected time points, 5 mL of the filtered waters were in addition transferred into Nalgene bottles containing 20 mL of MilliQ water for analysis of monomeric silica contents. The dilution ensures that further polymerisation of silica is prevented. After collection, the samples were stored at 3–6 °C for maximum 2 days before analysis of the dissolved gases and monomeric silica and for maximum 3 weeks for the analysis of cations or anions. Finally, at locations 1 to 3, two litres of separated water were filtered through ten pre-weighted 0.2 µm polycarbonate membranes to assess particles load, and separate 0.2 µm polycarbonate membranes were used to filter 100 mL to assess particle sizes, shapes and distribution via electron microscopic imaging All membranes were dried at 40 °C for ~16 h and re-weighed.

2.2. Analyses of separated water

Chloride was analysed by ion chromatography (IC) using a Thermoscientific Dionex system DX600, equipped with a AG16 (2 × 5 mm) and AS16 (2 × 250 mm) column, with an analytical uncertainty of ± 5%, based on multiple standard measurements. The concentrations of the major cations (Al, Ca, K, Na, Si) were analysed by inductively coupled plasma optical emission spectrometry (ICP-OES, Thermo Scientific iCAP7400; analytical uncertainty of < 4% based on multiple standard measurements) while the trace cations (Mg, Fe) were analysed by inductively coupled plasma mass spectrometry (ICP-MS, Thermo Scientific iCAPQc; analytical uncertainty of < 3% based on multiple standard measurements).

The concentrations of dissolved CO_2 and H_2S were analysed by total alkalinity titration (Metrohm 905 Titrando equipped with a Metrohm Aquatrode plus) and titration with mercury acetate using dithizone as an indicator, respectively (Arnórsson et al., 2006). The analytical uncertainties are ± 1% for total alkalinity titration and ± < 0.1% for titration of H_2S. The monomeric silica content was analysed based on the method described by Gunnarsson et al. (2010) using a JENWAY 6300 spectrophotometer. In addition to total and monomeric silica, "polymeric" silica was determined by subtracting the concentration of monomeric silica from the total silica concentration (< 0.2 µm filtered fraction).

2.3. Analyses of precipitates on scaling plates and filter membranes

The materials deposited on the scaling plates and filter membranes were analysed by field emission gun scanning electron microscopy (FEG-SEM, FEI Quanta 650 at 15 keV, coated with ~40 nm of gold). Selected, non-coated filter membranes were also imaged at ultra-high resolution, using a low kV cold-field emission scanning electron microscope (CFE-SEM, Hitachi SU8230 at 2 kV). The FEG-SEM images were used to determine the dimensions of the observed structures by measuring widths and lengths of 70–100 structures or particles that had formed or were deposited in the top side of each plate or filter

Table 2
Average and standard deviation (as 1 SD) of temperature, fluid composition, pH, Eh and salinity as determined for the different fluid samples (n = 9) at each of the four sampling locations.

		Loc. 1	Loc. 2	Loc. 3	Loc. 4
Temperature	[°C]	117.8 ± 0.4	56.6 ± 1.6	58.0 ± 5.3	72.5 ± 11.2
Flow rate	[L/s]	416 ± 54	420 ± 51	282 ± 18	430 ± 29
SiO_2	[mg/L]	802 ± 19	801 ± 30	794 ± 30	550 ± 76
Na	[mg/L]	204 ± 8	205 ± 9	207 ± 8	140 ± 10
Cl	[mg/L]	173 ± 12	171 ± 9	175 ± 6	120 ± 5
K	[mg/L]	34.7 ± 1.6	34.7 ± 1.7	35.1 ± 1.6	23.6 ± 1.2
CO_2	[mg/L]	25.4 ± 5.5	25.2 ± 4.8	23.8 ± 3.7	18.5 ± 3.8
H_2S	[mg/L]	19.2 ± 2.9	19.8 ± 2.5	20.5 ± 1.9	14.3 ± 2.7
Al	[mg/L]	1.99 ± 0.09	2.04 ± 0.11	2.04 ± 0.11	1.36 ± 0.07
Ca	[mg/L]	0.71 ± 0.13	0.70 ± 0.06	0.71 ± 0.04	0.50 ± 0.06
Fe[a]	[µg/L]	7.6–27.8	3.1–51.5	5.7–58.9	5.4–98.3
Mg[a]	[µg/L]	3.2–70.1	< 1.1–42.5	< 1.1–42.2	1.4–52.4
pH meas.[b]	–	9.4 ± 0.2	9.4 ± 0.2	9.4 ± 0.2	9.1 ± 0.3
pH calc.[c]	–	8.5 ± 0.1	9.0 ± 0.1	9.0 ± 0.1	8.8 ± 0.2
Eh[c]	[V]	−0.56 ± 0.01	−0.46 ± 0.01	−0.47 ± 0.01	−0.48 ± 0.02
Salinity[d]	[%]	0.06	0.05	0.05	0.04

[a] The concentrations of Fe and Mg are reported as ranges rather than averages ± 1 SD due to the large variations in concentrations measured. These variations can stem from (a) corrosion of the steel pipes and redox effects for Fe and (b) precipitation of Fe- and Mg- containing alumosilicates. These variations do not affect or change the silica precipitation and are thus not considered further.
[b] As measured at. 21–27 °C.
[c] Derived from PHREEQC simulations at measured *in situ* temperatures and with the analysed fluid compositions.
[d] Calculated based on the specific conductance derived from PHREEQC and the temperatures listed in this table.

manually.

The elemental composition of the precipitates was determined by energy dispersive spectroscopy (EDS; AZtec software, Oxford Instruments, Version 2.2). From the scaling plates onto which enough material had precipitated, material was scraped off and analysed by X-ray diffraction (XRD; Bruker D8 diffractometer, $CuK_{\alpha 1}$; 5–90° 2θ; 0.01°/step; data evaluation by the EVA software, Bruker, Version 3.0). XRD analyses of the materials on the filter membranes was done with the filters glued directly onto the XRD silicon holders.

The internal structure, composition and thickness of the precipitates on the scaling plates from location 1 were investigated via two approaches. For high resolution work, sections (15 × 10 × 0.15 µm) were prepared by focused ion beam (FIB) milling at the German Research Center for Geosciences (GFZ) Potsdam, Germany from the 1 day, 3 day and 1 week scaling plates following the method described by Wirth (2009). The FIB foils were analysed using a high-resolution transmission electron microscope (HR-TEM, TECNAI F20 X-Twin, 200 kV) at GFZ equipped with a Gatan Tridiem Imaging Filter and an EDAX X-ray analyser. Secondly, all scaling plates from location 1 (1 day to 10 weeks) were embedded in epoxy resin, cut along the width of the scaling plates and polished before being imaged by FEG-SEM as described above.

2.4. Geochemical simulations

The composition of the separated waters as well as the measured pH and temperatures were used as input parameters for geochemical simulations using PHREEQC (version 3.0, Parkhurst and Appelo, 2013) with the phreeqc.dat database, updated with the thermodynamic data for amorphous silica solubilities from Gunnarsson and Arnórsson (2000). Simulations were conducted to derive the *in-situ* pH and Eh conditions and the saturation indices (SI) of the compounds of interest in the geothermal fluid.

2.5. Determination of precipitation rates

The precipitation rates were evaluated via two approaches: (1) we quantified the amount of material deposited on each plates (in mg) from the 1 day, 3 day and 1 week deployments at each location and (2) we measured the average thickness of the precipitation layer for the 1 week and longer deployments at location 1 only.

For the first approach, the precipitated amount was measured by weighting of the scaling plates before and after the deployments and converted to a volume using a density of $\rho_{SiO2} = 2.25\,mg/mm^3$ for a high density vitreous silica scale (Mroczek et al., 2011). Assuming that the layers were all made of silica and that they were of roughly constant thickness around the plate, the thickness of the precipitates was calculated. We then used the mass of silica precipitated and the surface areas of the individual scaling plates to calculate precipitation rates. Based on an average precipitation rate determined for the deployments up to 1 week, the thickness of the precipitated silica layer was calculated from linear extrapolations for the longer deployments. In order to evaluate the validity of such a linear extrapolation, the thickness of silica layers on all plates from location 1 (from 1 to 10 weeks) were measured on the FIB sections and the epoxy-embedded samples by HR-TEM and FEG-SEM respectively (as described above). The thickness of each precipitated silica layer was measured at multiple locations around each plate (n = 36–113) to derive an average value. Using the same $\rho_{SiO2} = 2.25\,mg/mm^3$, the mass of silica was calculated and converted to a precipitation rate.

3. Results

3.1. Composition of separated water

The four sampling locations differed with respect to fluid temperature, flow rate and fluid composition (Table 2). This was in a large part defined by their position within the Hellisheiði geothermal power station (Fig. 1). Location 1 (before the heat exchangers) was characterised by fluids with temperatures of around 118 °C and a flow rate of nearly 420 L/s. The separated water at this location was a low salinity NaCl fluid containing ~800 mg/L SiO_2, ~25 mg/L $CO_{2(aq)}$ and ~20 mg/L $H_2S_{(aq)}$. The measured pH was 9.4, the calculated pH at the *in situ* temperature was 8.5 and the Eh −0.56 V.

At location 2, after the separated water was cooled inside the heat exchanger (Fig. 1), the fluid temperature was lower (~57 °C) but the flow rate and the fluid composition remained identical to location 1. The measured/calculated pH was 9.4/9.0 and the calculated Eh −0.46 V. These same conditions prevailed at location 3, further downstream from the heat exchangers (Fig. 1) but the flow rate was

Table 3
Silica speciation in the separated water at Hellisheiði.

			Loc. 1	Loc. 2	Loc. 3	Loc. 4
Total concentration SiO_2		[mg/L]	802 ± 19	801 ± 30	794 ± 30	550 ± 76
Solubility[a]		[mg/L]	465	204	209	261
SI[b] amorphous SiO_2		[−]	0.10 ± 0.02	0.44 ± 0.02	0.42 ± 0.02	0.18 ± 0.08
Speciation						
Monomeric[c]		[%]	85.0	81.4	75.5	85.8
"Polymeric"[d]		[%]	15.0	18.6	24.5	14.2
Particulate[e]		[%]	< 0.02	< 0.03	< 0.03	n/a
Particle sizes [μm][f]						
on the filters	mdn	[μm]	0.2	0.1	0.1	n/a
	IQR	[μm]	(0.1–0.3)	(0.1–0.3)	(0.1–0.2)	
on the plates	mdn	[μm]	3.4	0.8	1.0	0.9
	IQR	[μm]	(1.7–6.8)	(0.4–1.7)	(0.4–1.7)	(0.5–3.1)

[a] Calculated based on Gunnarsson and Arnorsson (2000).
[b] Saturation index, derived from PHREEQC simulations using the *in-situ* temperatures and with the fluid compositions given in Table 2.
[c] Determined by analysing filtered (0.2 μm) and diluted sample aliquots using the spectrophotometric molybdate method.
[d] Determined from subtracting the concentration of monomeric silica from the concentration of total silica (Table 3).
[e] Determined from the weight difference of the 10 filter membranes before/after sampling and a density of 2.25 mg/mm^3 for glass-like, high density amorphous silica (Mroczek et al., 2011).
[f] Determined from manual measurement of silica particles in FEG-SEM images found on filter membranes or scaling plates; mdn = median, IQR = interquartile range (n = 70–100 particles per scaling plate or filter).

much lower (~280 L/s) due to the differences in pipe geometry. Just after location 3, steam condensate was added to the fluid (around 0.4 L of condensate per 1 L of separated water). The condensate was hotter than the separated water, thus the temperature of the fluid at location 4 was higher (~73 °C). The addition of the condensate downstream of location 3 and differences in pipe geometry resulted in the highest measured flow rate (Table 2). The biggest effect of the mixing with condensate (= almost pure water) was on the chemistry as it resulted in the concentrations of all fluid components and the pH being lower at location 4.

The saturation index calculations revealed that the separated waters were supersaturated with respect to amorphous silica at all locations (Table 3). The total silica reported in Table 2 represents the sum of all silica species: monomers (H_4SiO_4), oligomers/polymers (dimers, trimers, tetramers etc.) and (nano) particulate silica < 0.2 μm. Partitioning the various silica species reveals that in all cases monomeric silica was by far the dominant component (Table 3). The proportion of monomeric silica decreased along the flow path from 85% down to 75% from location 1 to 3. At the same time, the proportion of polymeric silica increased from 15 to 25% due to continuous polymerisation. At location 4, the dilution by the addition of steam condensate caused the percentage of monomeric silica to increase to 86%.

XRD analyses and imaging of the filter residues revealed that they consisted of amorphous silica particles. The proportion of particulate silica retained by the filter membranes, as evaluated from the difference in weight of the filters, accounted for less than 0.05% of the total silica (Table 3) at all locations. The particles on the filters had a mean diameter identical or smaller than the pore sizes of the filter membranes (0.2 μm), yet particle sizes varied between < 0.1 μm and in some exceptional cases over 20 μm. The particles could be subdivided into two groups: (1) particles with a relatively smooth surface (Fig. 2A & B, marked a) and (2) particles consisting of aggregates of much smaller and rougher surfaced particles (0.01–0.05 μm; Fig. 2A & B, marked b). In addition, at locations 1 to 3, a few platy Al-Si containing phases were identified (Fig. 2A) by FEG-SEM EDS and confirmed as alumosilicates, specifically clinochlor by XRD. At location 4, silica particles were very rare and the abundance of chlorite minerals such as chamosite and clinochlore and the magnesium silicate sepiolite (identified by XRD, FEG-SEM EDS analyses and PHREEQC simulations) was high (Fig. 2C).

3.2. Composition and structure of precipitates on scaling plates

The majority of the precipitates on the deployed scaling plates were identified as amorphous silica by XRD and EDS spot analyses. These amorphous silica precipitates were rarely interspersed with other mineral and metal flakes, identified as alumosilicates (based on FEG-SEM EDS) and in some samples confirmed to be clinochlore (by XRD). In addition to these alumosilicates, EDS analyses also revealed that the silica was not pure but most often peaks for various ions from the geothermal fluid (Na, Cl, S, Al, Fe etc.) were observed associated with the silica precipitates.

The scaling plates were completely covered by a layer of amorphous silica, even after just 1 day. This layer was very dense and it lacked any internal structure (Fig. 3A & B). The average thickness of the silica layer was the same around each plate and no differences between the individual faces of the plates (top vs. bottom, main face vs. edge) were observed. The layer thickness increased over time; for example, it increased from 0.3 μm to > 20 μm over 10 weeks on the plates deployed at location 1. The surface of the precipitation layer was uneven with a botryoidal texture consisting of individual half-spheres (Fig. 3C & D) which grew in size over time (Fig. 4; evaluated through measurement of lengths and widths) but the number of spheres decreased per area of plate.

At all four locations rapid growth of the half-spheres during the 1 day to 2 week deployments was followed by reduced growth rates for the longer deployments. The increase in area of the half-spheres was fastest at locations 1 and 2, where the area of individual half-spheres increased from 0.05 μm^2 after 1 day to around 75 μm^2 at 10 weeks. At location 3, the growth was slower with the maximum area of half-spheres only reaching 15 μm^2. Although silica half-spheres were also observed at location 4, their growth was very slow and even after 10 weeks they only reached areas of 0.1 μm^2. In all samples, measurements were carried out on the top side of the scaling plates, yet for the 1 week deployment the areas of the half-spheres were also measured on the bottom side of the scaling plates at all four locations to confirm that the average areas on both sides were identical (open symbols in Fig. 4).

In many cases, on top of the botryoidal silica layer, individual or merged silica particles were observed (Fig. 5). These spherical particles looked identical to the particles found on the filters (Fig. 2), but on average, they were markedly larger (Table 3). The spatial distribution of the particles on the plates was completely random with some plates containing only few particles, while other having larger areas covered

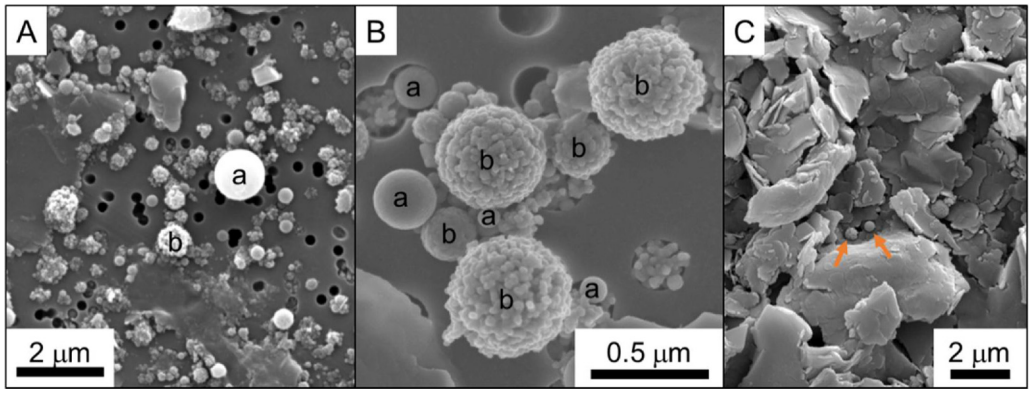

Fig. 2. FEG-SEM images of 0.2 µm polycarbonate filter membranes with (A & B) two types of silica particles (smooth particles marked a and rough particle aggregates marked b) from location 1 and (C) platy alumosilicates with very few and very small silica spheres (arrows) from location 4.

by silica particles. In some instances, neighbouring particles were cemented together (Fig. 5A) or to the surface of the existing silica layer (Fig. 5B) by the deposition of dissolved silica. A very small number of these individual silica particles became embedded into the botryoidal surface layer (Fig. 5C).

Another mode of silica particle deposition was as 3D aggregates that had fan- to ridge-shaped structures (Fig. 6A–C), pointing towards the direction of the flow and that were cemented together (Fig. 6D). These microstructures were exclusively found on the top face and along the plate edges oriented towards the flow in the 2, 4 and 10 week deployments (Fig. 6A). During the 2 week deployment at location 1, single fans reached a maximum of 300 µm in height. During the 4 week deployment, the fans grew to 700 µm in height (Fig. 6A) while on the 10 week scaling plate from this location, the fans had merged into ridges that were up to 10 mm long and 1 mm high (Fig. 6B & C). At locations 2 and 3, fewer and smaller fans (maximum 300 and 500 µm after 4 and 10 weeks, respectively; no fans after 2 weeks) were observed. Interestingly, during the 6 week deployment, independent of the location, no 3D structures were observed to have grown on the ubiquitous botryoidal silica layer.

4. Discussion

4.1. Precipitation pathways

We observed two different silica textures on the scaling plates (Figs. 3 and 6): dense silica layers with a botryoidal surface and individual silica particles cemented into 3D structures. While the silica layers were identified on all scaling plates and grew continuously in thickness, the 3D structures were only observed during the 2, 4 and 10 week long deployments and never at location 4, indicating that their formation was controlled by different processes and precipitation pathways.

The botryoidal silica layers formed by heterogeneous nucleation and growth on/at the steel-fluid-interface. All plates were made of the same non-polished S316 stainless steel (Fig. 1C & D) and in all cases botryoidal layers covered the steel surfaces completely, even during the 1 day deployment. Thus, the plate surface properties were not a reason for the observed differences in layer thickness (Fig. 3) or size of half-spheres (Fig. 4) between locations. These differences are a consequence of the changing silica precipitation depending on local physicochemical conditions. The surface of the half-spheres appeared smooth (Fig. 3)

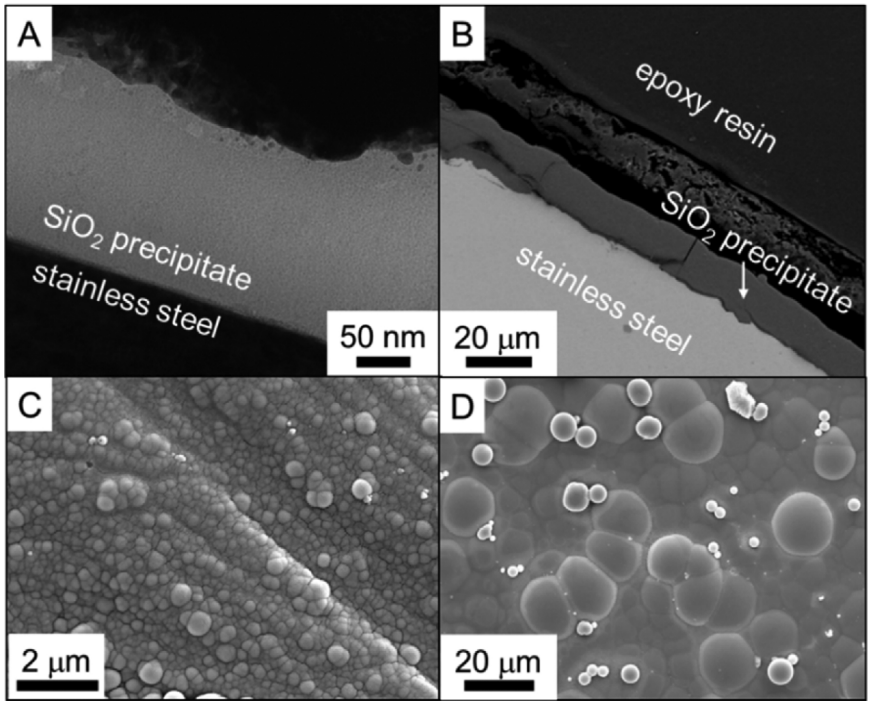

Fig. 3. Electron microscope images showing a cross section of the precipitation layer after (A) 1 day (FIB section imaged by TEM) and (B) 10 weeks (FEG-SEM image of a sample embedded in epoxy resin, cut perpendicular to the plate). FEG-SEM images of the surface of scaling plates deployed for (C) 1 day and (D) 10 weeks, respectively. All samples were from location 1. Note the difference in scale.

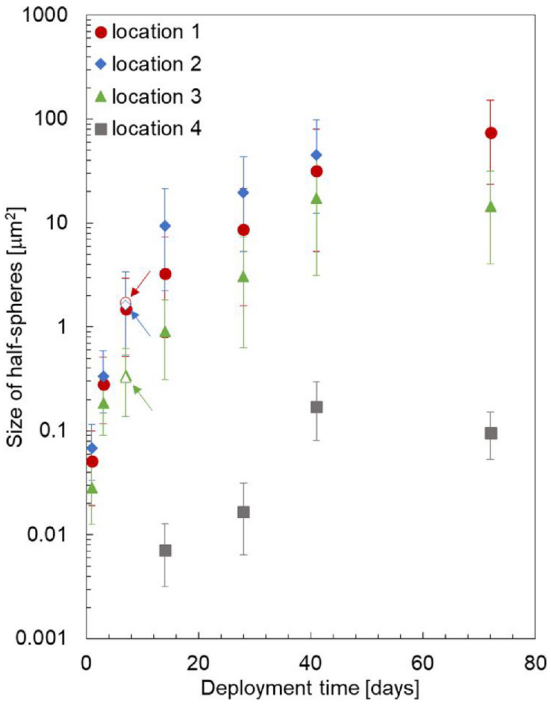

Fig. 4. Increase in the average area of the half-spheres over time at all four locations as evaluated based on measured lengths and widths of between 70 and 100 half-spheres on each plate. No 10 week sample was recovered at location 2. The empty symbols (highlighted by arrows) represent the sizes of the half-spheres measured on the underside of the 1 week deployment at locations 1 to 3. Note the logarithmic scale on the y-axis.

and the scarcity of homogeneously formed particles (partly) embedded in the silica layer (Fig. 5C) suggests that the growth primarily occurred by addition of dissolved silica from the fast flowing fluid, likely monomers. This is in line with results from previous studies (Bohlmann et al., 1976; Bremere et al., 2000; Mroczek and McDowell, 1988), which suggested that at neutral to slightly alkaline pH growth occurs primarily via monomeric silica addition due to the negative surface charge of larger species and the resulting electrostatic repulsion.

The attachment of monomers to pre-existing silica surfaces follows the same mechanism as silica polymerisation and growth is thus naturally enhanced when polymerisation rates are high (i.e., at high total silica concentrations, high percentage of monomers, elevated temperature and alkaline pH; Alexander et al., 1954; Bremere et al., 2000; Gunnarsson and Arnórsson, 2005; Icopini et al., 2005; Weres et al., 1981). This explains why the growth rate of the half-spheres is highest at location 1 (Fig. 4). The fluid at location 1 had a high concentration of total silica (~800 ppm), a high percentage of silica monomers (85%) as well as the highest temperature (~120 °C), facilitating rapid attachment of monomeric silica from solution onto the scaling plates. Location 2 shows identical total silica concentrations, but a somewhat lower monomeric silica content (81%) and a lower temperature (~60 °C), explaining why the growth of the half-spheres as a function of time is slower. At location 3 on the other hand, the total silica content and fluid temperature were equal to location 2 but the fluid contained an even lower percentage of silica monomers (~76%) and thus an even slower growth of the half-spheres. Finally, location 4 was characterised by the lowest growth rate for the half-spheres (Fig. 4). The fluid at this location was characterised by a higher temperature than at location 2 and 3 (~73 °C) and the highest monomer content (86%) of all locations. However, the substantially lower total silica concentration (~550 ppm) was likely the reason for the much slower growth rate, suggesting that the total silica concentration was the dominant factor in controlling polymerisation rate of silica and thus attachment and growth of the half-spheres. This is in agreement with previous studies (Gunnarsson and Arnórsson, 2005; Icopini et al., 2005; Weres et al., 1981). The same studies also report a strong dependence of silica precipitation on pH. However, the pH variation between the four locations in this study was only half a pH unit (Table 2) and thus no marked effect of pH on silica precipitation was observed. The effect of gravity was also investigated by not only measuring the half-spheres on the top sides of the plates but also on the bottom sides (Fig. 4). The half-spheres on both sides were identical at all locations, indicating that gravity had no effect, an observation which is in line with heterogeneous nucleation and subsequent growth by monomer addition.

The reduced growth of the silica half-spheres as a function of deployment time (Fig. 4) and the decrease in absolute numbers due to merging (Fig. 3C & D and Fig. 7) is a consequence of preferential deposition of silica at half-sphere boundaries. Such intersections show an infinitely small negative radius of curvature and thus a solubility of zero (Iler, 1979). This relationship suggests that the growth of the silica layer was controlled by the rate of attachment of monomeric silica from the solution and not diffusion controlled, which is in line with previous studies (Bohlmann et al., 1980; Crerar et al., 1981; Weres et al., 1981).

The 3D structures on the other hand were composed of individual silica particles, which formed through homogeneous nucleation in the fluid. Once a nucleus formed, it grew by addition of monomeric silica until it reached its optimal size (Fig. 7). Homogeneous nucleation and particle growth were only controlled by the physicochemical conditions of the fluid. Under ambient conditions and up to 60 °C particles grow to ≤10 nm in laboratory experiments (Goto, 1956; Icopini et al., 2005; Iler, 1979; Tobler and Benning, 2013; Tobler et al., 2009). However, at alkaline pH and in the absence of salts, particles can grow to sizes of 100 nm (Iler, 1979). While this could explain the presence of the smallest particles observed on the filter membranes (Fig. 2B), it does not explain the particles with diameters of several micrometres and

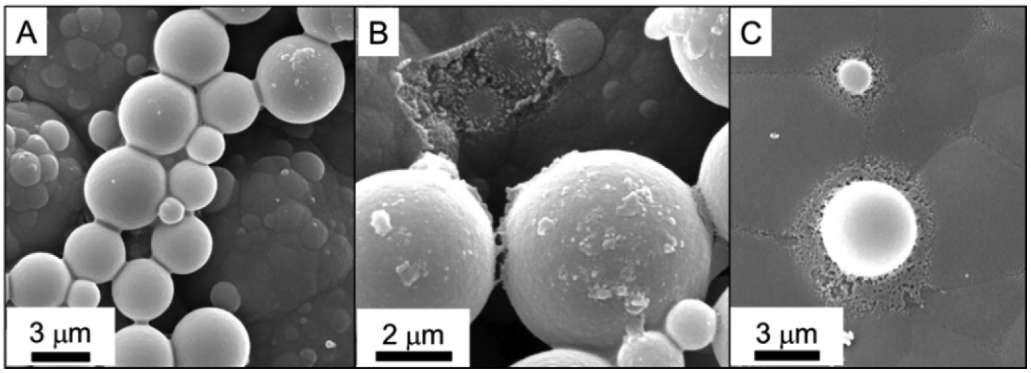

Fig. 5. FEG-SEM images showing particles deposited onto the botryoidal silica layer where they were (A) cemented together and/or (B) cemented to the surface or (C) (rarely) incorporated into the botryoidal silica layer. Images from locations 1 and 2.

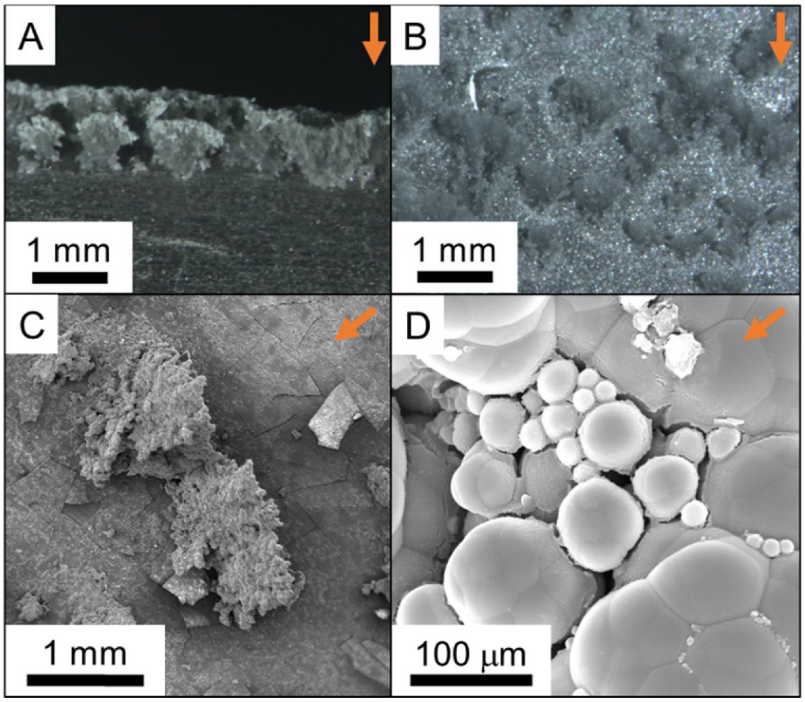

Fig. 6. Microphotographs showing the 3D, fan-shaped structures found at location 1 following the 4 and 10 week deployments. Images (A) shows the edge of the plate and (B) the surface of the plate. The fans (C) consisted of spherical silica aggregates that grew as a function of time seemingly by addition of individual particles that were then cemented together (D). Flow direction indicated by arrows.

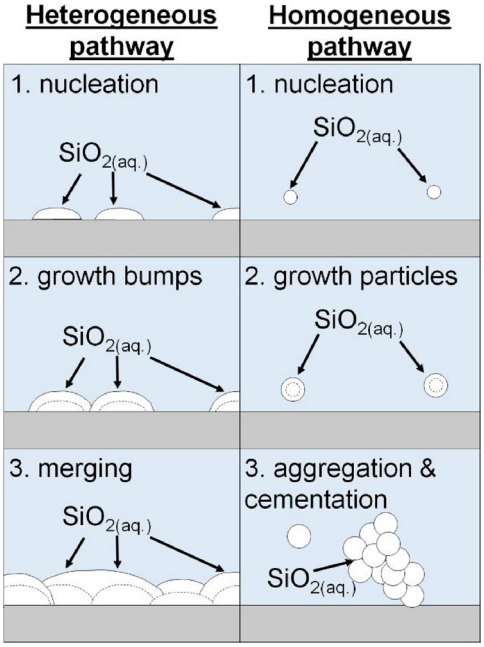

Fig. 7. Schematic of the two silica precipitation pathways ($SiO_{2\ (aq)}$ = silica monomers in solution) as they occur inside the pipelines of the Hellisheiði geothermal power plant.

smooth surfaces (Fig. 2A). They likely formed due to the favourable conditions for growth inside the pipelines (alkaline pH, elevated temperature, constant re-supply of dissolved silica and at low salt concentrations) which are similar to the conditions in the industrial "build-up process", developed for the production of large particle silica sols (Morris and Vossos, 1970). In addition, the fast flow rates inside the pipelines favour the transport of larger particles without deposition. However, these large particles only account for a small proportion of the total particulate silica in the fluid. Nevertheless, they are of importance as they are preferentially deposited as shown by the larger average particle size on the plates compared to the filters (Table 3). The difference is most pronounced at location 1 and smaller at locations 2 and 3, indicating that the particles grew larger at higher temperatures and/or that the fluid got depleted with respect to large particles along the flow path, despite the high flow rate. Both factors also explain why such particles were rare at location 4.

As the separated water also contained low concentrations of multivalent cations (Table 2), they potentially acted as flocculants between the negatively charged silica particles leading to some particles becoming aggregated into larger particles (Fig. 2B) and the formation of 3D fan- and ridge-shaped structures (Fig. 6) very similar to the dendritic precipitates predicted in hydrodynamic simulations (Hawkins et al., 2013, 2014). Within these 3D structures, the individual particles were cemented together by monomeric silica from solution (Fig. 6). This occurred in the embayment between particles (Chigira and Watanabe, 1994; Rimstidt and Cole, 1983), where the solubility of amorphous silica is zero due to the infinitely small negative radius of curvature at the contact point (Iler, 1979). The 3D structures grew largest at location 1, likely due to the larger average size and higher number of particles, and were absent at location 4 where there were only few silica particles in the fluid (Table 3). The 3D structures only grew during the 2 week (only location 1), 4 week (locations 1 + 2) and 10 week (locations 1 to 3) deployments. This indicates that deployment time as well as particle numbers and/or sizes (both highest at location 1) were the crucial factors controlling growth of these 3D structures. Interestingly, the fan- and ridge-shaped structures were not observed during the 6 week deployment. This was due to the much higher average flow rate of 516 L/s at locations 1 and 2 (compared to 416 L/s measured during the other deployments, Table 2) recorded during this deployment. While the reason for this substantial increase in flow rate is unknown, it indicates that a threshold flow rate exists, above which not enough particles are deposited for such 3D structures to form.

Silica precipitates with morphologies similar to the botryoidal silica layers and 3D particle aggregates described here for the Hellisheiði pipelines, were also described at other power plants in Iceland and New Zealand (Brown and McDowell, 1983; Carroll et al., 1998; Gudmundsson and Bott, 1979; Rothbaum et al., 1979; Thórhallsson et al., 1975), in silica sinters from Iceland (Jones and Renaut, 2010) and in laboratory experiments mimicking the growth of silica veins (Okamoto et al., 2010). This indicates that the silica precipitation

Table 4
Thickness of the botryoidal silica layer based on the difference in pre- and post-deployment weights of scaling plates.

	Amount of silica precipitated		Thickness of layer [μm][c]	Precipitation rate [mg m^{-2} day^{-1}][d]
	[mg][a]	[mm^3][b]		
Location 1				
1 day	2.5	1.1	0.5	1027
3 days	5.7	2.5	1.0	768
1 week	13.2	5.9	2.4	766
Location 2				
1 day	2.8	1.2	0.5	1124
3 days	5.6	2.5	1.0	756
1 week	12.3	5.5	2.2	717
Location 3				
1 day	2.0	0.9	0.4	803
3 days	5.8	2.6	1.0	783
1 week	11.4	5.1[e]	1.7	663
Location 4				
1 day	0.8	0.3	0.1	315
3 days	0.6	0.3	0.1	82
1 week	3.2	1.4[e]	0.5	189

[a] Calculated based on the weight difference of the scaling plate before and after deployment.

[b] Calculated based on a density of 2.25 mg/mm^3 for glass-like, high density amorphous silica (Mroczek et al., 2011).

[c] Calculated assuming a constant thickness of the silica layer around the whole plate.

[d] Calculated using the amount precipitated and the surface area of the scaling plates. The average of the 3 day and 1 week rates was used for the extrapolation of the thickness of the silica layer to 10 weeks (Fig. 8A).

[e] Scaling plates 2.5 cm wide (all other scaling plates were 2 cm wide). Taken into account when calculating the thickness of the layer and the precipitation rate.

mechanisms described here operate over a wide range of physico-chemical conditions and different geological settings.

4.2. Quantification of precipitation rates

The precipitation rates could only be determined for the heterogeneous pathway and the formation of the botryoidal layer due to the strong dependency on flow rate and thus more erratic deposition behaviour of the homogeneous pathway.

Initially, we determined the amount of silica deposited on the scaling plates by weight up to the 1 week deployment. The amount increased four- to five-fold from 1 day to 1 week at all locations (Table 4), yet the absolute mass deposited differed substantially between the four locations. The total accumulated silica was highest at location 1 (13.2 mg) and slightly lower at locations 2 (12.3 mg) and 3 (11.4 mg). Substantially less silica (3.2 mg) was deposited at location 4 during the same time interval. As for the growth of the half-spheres (Fig. 4), the differences between the locations could be explained by changes in physicochemical conditions affecting the attachment of dissolved silica from the fluid (i.e. silica concentration and monomer content as well as temperature). The mass of silica deposited was used to calculate the thickness of the formed silica layer and determine precipitation rates. The botryoidal silica layers ranged from 1.7 to 2.4 μm at locations 1 to 3 and only 0.5 μm at location 4. The determined precipitation rates strongly decreased from the 1 day to the longer deployments (Table 4). This was due to the changing interactions controlling precipitation. Initially, deposition took place at the steel-fluid interface and was controlled by the steel surface properties (e.g. roughness) and the nucleation behaviour of silica. Once the surface was covered by silica nuclei, which happened at some point during the first 24 h of the deployments as evidenced by the continuous botryoidal layer found on all plates deployed for 1 day, precipitation was

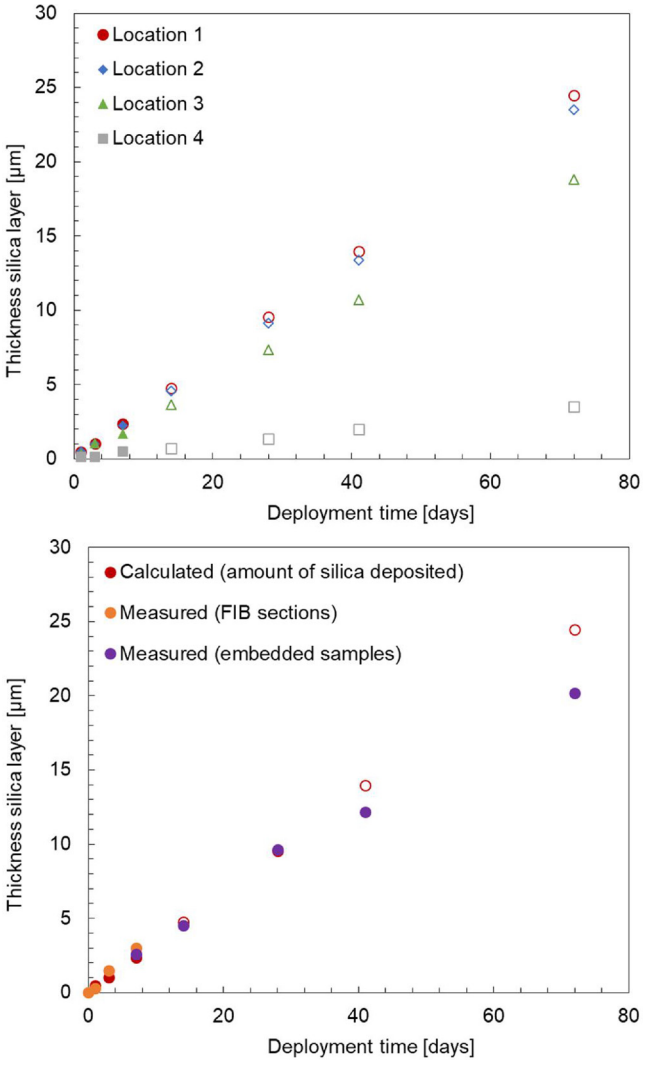

Fig. 8. Increasing thickness of the botryoidal silica layer over time: (A) calculated from the weight of silica and a density of 2.25 mg/mm^3 (Mroczek et al., 2011) at all locations up to 1 week (solid symbols) and linear extrapolations up to 10 weeks (empty symbols) and (B) derived from the weight of the scaling plates pre- and post-deployment (red) as well as thickness measurements from FIB sections (orange) and embedded samples (purple) by electron microscopy at location 1 (For interpretation of the references to colour in this figure legend, the reader is referred to the web version of this article).

controlled by silica-silica interactions only. The precipitation rates determined for the 1-day deployments (800 to over 1100 mg m^{-2} day^{-1} at locations 1 to 3 and 315 mg m^{-2} day^{-1} at location 4) were strongly influenced by the interactions between silica and the steel plates and thus do not represent the long-term precipitation behaviour of silica from the fluid. Therefore, these rates were not used to calculate an average precipitation rate for each location and linearly extrapolate the thickness of the precipitation layer to 10 weeks (Fig. 8A). However, as with the evolution of the size of the half-spheres (Fig. 4), it was expected to see a decrease in growth of this silica layer over time, meaning the extrapolation is representing a 'worst case' scenario rather than the behaviour of silica precipitation as a function of time.

In order to better constrain the time-dependant deposition of silica, precipitation rates up to 10 weeks were also determined at location 1 by measuring the thickness of the silica layer using FIB sections and by imaging plates embedded in epoxy resin and cut perpendicularly. The silica layer grew from 0.3 μm after 1 day to over 20 μm after 10 weeks (Table 5). The values of the shorter deployments are in good agreement

Table 5
Thickness of the precipitated silica layer at location 1 from FIB sections and samples embedded in epoxy as well as calculated precipitation rates.

	Measured [μm]		Amount of silica [mg][a]	Precipitation rate [mg m^{-2} day^{-1}][b]
	FIB sections	Embedded		
1 day	0.3	–	1.7	675
3 days	1.5	–	8.3	1125
1 week	3.0	2.6	16.6 / 14.4	965 / 836
2 weeks	–	4.5	24.9	725
4 weeks	–	9.6	53.2	773
6 weeks	–	12.2	67.4	669
10 weeks	–	20.2	111.7	632

[a] Calculated based on a density of 2.25 mg/mm^3 for glass-like, high density amorphous silica (Mroczek et al., 2011) and the volume of silica precipitated assuming a constant thickness of the precipitation layer all around the scaling plates.

[b] Calculated using the amount precipitated and the surface area of the scaling plates.

with the thicknesses calculated and extrapolated based on the amount of silica. For the longer deployments (6 and 10 weeks), the measured thickness was around 20% lower than the extrapolated value showing that the extrapolation indeed represents a 'worst case' scenario (Fig. 8B). The discrepancy is due to the steadily decreasing precipitation rates (Table 5), which are not taken into account in the linear extrapolation of the average precipitation rates. The decrease is caused by the disappearance of preferential deposition sites (i.e. half-sphere boundaries) over time due to continuous merging. This highlights the need for time-resolved and long-term studies (i.e. over weeks to months) to determine reliable precipitation rates of silica inside in-use geothermal power plants.

The above derived silica precipitation rates compare well with rates from other sites where the physicochemical conditions of the fluids are similar. This includes the Sumikawa power plant, Japan (Okazaki et al., 2017) and Ohaaki power station, New Zealand (Brown and McDowell, 1983) where silica precipitation rates of around 840 and 1300 to 1800 mg m^{-2} day^{-1} respectively were reported. However, care has to be taken to only compare processes, which are indeed similar. Mroczek et al. (2017) for example also studied silica precipitation at Ohaaki power station and reported much higher precipitation rates (up to 4500 mg m^{-2} day^{-1}), yet the precipitates were described by the authors as "wavy silica spicules" and these seem more akin to the 3D structures reported here, rather than the dense botryoidal layer from which we determined our precipitation rates. It is thus likely that the rates determined by Mroczek et al. represent the deposition rate of silica particles rather than silica precipitation via the heterogeneous pathway and cannot therefore be compared directly to the rates reported in this study. Care is also needed when comparing different precipitation settings. Several studies reported silica precipitation rates from *in situ* sinter growth experiments around hot springs or geothermal wastewater drains (Handley et al., 2005; Mountain et al., 2003; Tobler et al., 2008). The rates reported in these studies are generally higher than the ones reported for silica scaling inside geothermal power plants. For example, the rates reported from Krafla (Tobler et al., 2008) under physicochemical conditions comparable to the separated water studied here, are more than 50 times higher. This is because subaerial silica sinter formation occurs predominantly at the air-water interface where recurring wetting-evaporation cycles occur as well as other hydrodynamic processes including wave action, capillary action, diffusion and splash which enhance silica precipitation. In addition, the presence of microbes and biofilms also accelerates silica precipitation and thus increases the deposition rates compared with purely abiotic precipitation. The factors affecting silica precipitation most strongly are therefore vastly different in these settings compared to geothermal pipelines.

4.3. Implications on predicting silica scaling

Based on the growth of the half-spheres (Fig. 4) and the determined amounts of silica precipitated in this study (Tables 4 and 5) we can conclude that silica precipitation was fastest at locations 1 and 2 and slowest at location 4. This is in conflict with the saturation indices (SIs) calculated by PHREEQC (Table 3), which suggested that precipitation should be fastest at locations 2 and 3 (highest SIs = highest driving force for precipitation). However, the SI is a purely thermodynamic concept, which is only of limited use in a system as dynamic as a geothermal power plant where changes in the physicochemical conditions (e.g., cooling in the heat exchangers, dilution by steam condensate) occur rapidly and over short distances due to the fast flow rates. Therefore, it is also not surprising that our precipitation rates do not agree with theoretical calculations based on Rimstidt and Barnes (1980), which, when taking into account our solution composition and saturation indices derived from PHREEQC, yielded theoretical precipitation rates of 0.35–0.75 mg m^{-2} day^{-1}. However, even if we were to take kinetics into account to simulate the precipitation, the accuracy of our extrapolation predictions would likely not improve as the kinetics of silica polymerisation and silica (nano)particle formation are still highly contentious (reviewed by Tobler et al., 2017). This lack of predictability is a major issue in the development of geothermal resources as it is commonly cheaper and easier to keep the fluid at temperatures high enough to prevent silica supersaturation rather than to mitigate substantial silica scaling during operation.

5. Summary

In this study, we evaluated for the first time silica precipitation rates and mechanisms inside pipelines of an in-work high-entropy geothermal power station in a time resolved manner, showing how a well-constrained geothermal power plant is a prefect study site for mineral precipitation. Our results documented that amorphous silica precipitates via two pathways at Hellisheiði: (1) rapid heterogeneous nucleation of silica on any exposed surface resulting in half-spheres which, by addition of monomeric silica from solution, grow into a botryoidal silica layer and (2) homogeneous nucleation of nano- and micro-particles in the fast flowing fluid, followed by their growth and deposition on the pre-existing botryoidal layers leading to 3D fan- and ridge-shaped structures. Both pathways are predominantly controlled by total silica concentration, silica monomer content and temperature, while particle deposition is also strongly affected by hydrodynamics. Observations from other geothermal systems suggest that these precipitation modes are not unique to Hellisheiði but occur over a wide range of different conditions.

Acknowledgments

This research was made possible by Marie Curie grants from the European Commission in the framework of the MINSC Initial Training Research network [Project number 290040] to Liane G. Benning and Caroline L. Peacock and the framework of the NanoSiAl Individual Fellowship [Project No. 703015] to Tomasz Stawski. Daniela B. van den Heuvel acknowledges financial support by the International Geothermal Association (IGA) in the framework of the 2014 PhD Student Grant. Tomasz Stawski and Liane G. Benning also acknowledge the financial support of the Helmholtz Recruiting Initiative. We thank T. Windross and S. Burgess for preparation of all scaling plates and H. Bergmann for his help with the deployments at Hellisheiði power plant. We are grateful for the fluid analyses done at Reykjavik Energy and by S. Reid and F. Keay at the University of Leeds. We thank A. Schreiber and R. Wirth at the GFZ Potsdam for preparation of FIB foils and subsequent analyses by TEM. We also acknowledge analytical support by L. Neve (XRD) and R. Walshaw (SEM), both University of Leeds. We would like to thank H. Williams (University of Leeds), Th. Aebi and N.

Lötscher (both University of Bern) for help with embedding of the samples in resin and the subsequent cutting and polishing.

References

Alexander, G.B., Heston, W., Iler, R., 1954. The solubility of amorphous silica in water. J. Phys. Chem. 58, 453–455.

Arnórsson, S., 1975. Application of the silica geothermometer in low temperature hydrothermal areas in Iceland. Am. J. Sci. 275.

Arnórsson, S., Bjarnason, J.Ö., Giroud, N., Gunnarsson, I., Stefánsson, A., 2006. Sampling and analysis of geothermal fluids. Geofluids 6, 203–216.

Benning, L.G., Waychunas, G.A., 2007. Nucleation, growth, and aggregation of mineral phases: mechanisms and kinetic controls. Kinetics of Water-Rock Interaction. Springer, pp. 259–333.

Bohlmann, E., Shor, A., Berlinski, P., 1976. Precipitation and Scaling in Dynamic Geothermal Systems. Oak Ridge National Laboratories p. 21680.

Bohlmann, E.G., Mesmer, R.E., Berlinski, P., 1980. Kinetics of silica deposition from simulated geothermal brines. Soc. Pet. Eng. J. 20, 239–248.

Braunstein, D., Lowe, D.R., 2001. Relationship between spring and geyser activity and the deposition and morphology of high temperature (& 73 C) siliceous sinter, Yellowstone National Park, Wyoming, USA. J. Sediment. Res. 71, 747–763.

Bremere, I., Kennedy, M., Mhyio, S., Jaljuli, A., Witkamp, G.-J., Schippers, J., 2000. Prevention of silica scale in membrane systems: removal of monomer and polymer silica. Desalination 132, 89–100.

Brown, K., McDowell, G., 1983. pH control of silica scaling. In: Proceedings of the 5th New Zealand Geothermal Workshop. New Zealand. pp. 157–161.

Cady, S., Farmer, J., 1996. Fossilizationprocessesin siliceous thermal springs: trends in preservation along thermal gradients. Evol. Hydrotherm. Ecosyst. Earth Mars 150–173.

Carroll, S., Mroczek, E., Alai, M., Ebert, M., 1998. Amorphous silica precipitation (60 to 120 C): comparison of laboratory and field rates. Geochim. Cosmochim. Acta 62, 1379–1396.

Chigira, M., Watanabe, M., 1994. Silica precipitation behavior in a flow field with negative temperature gradients. J. Geophys. Res.: Solid Earth 99, 15539–15548.

Crerar, D.A., Axtmann, E.V., Axtmann, R.C., 1981. Growth and ripening of silica polymers in aqueous solutions. Geochim. Cosmochim. Acta 45, 1259–1266.

Dixit, C., Bernard, M.-L., Sanjuan, B., André, L., Gaspard, S., 2016. Experimental study on the kinetics of silica polymerization during cooling of the Bouillante geothermal fluid (Guadeloupe, French West Indies). Chem. Geol. 442, 97–112.

Dugger, D.L., Stanton, J.H., Irby, B.N., McConnell, B.L., Cummings, W.W., Maatman, R.W., 1964. The Exchange of twenty metal ions with the weakly acidic silanol group of silica Gel1, 2. J. Phys. Chem. 68, 757–760.

Fleming, B.A., 1986. Kinetics of reaction between silicic acid and amorphous silica surfaces in NaCl solutions. J. Colloid Interface Sci. 110, 40–64.

Fleming, B., Crerar, D., 1982. Silicic acid ionization and calculation of silica solubility at elevated temperature and pH application to geothermal fluid processing and reinjection. Geothermics 11, 15–29.

Fournier, R., Rowe, J., 1966. Estimation of underground temperatures from the silica content of water from hot springs and wet-steam wells. Am. J. Sci. 264, 685–697.

Gallup, D.L., 1997. Aluminum silicate scale formation and inhibition: scale characterization and laboratory experiments. Geothermics 26, 483–499.

Goto, K., 1956. Effect of pH on polymerization of silicic acid. J. Phys. Chem. 60, 1007–1008.

Gudmundsson, J.S., Bott, T.R., 1979. Deposition of silica from geothermal waters on heat transfer surfaces. Desalination 28, 125–145.

Gunnarsson, I., Arnórsson, S., 2000. Amorphous silica solubility and the thermodynamic properties of H_4SiO_4 in the range of 0 to 350 C at P_{sat}. Geochim. Cosmochim. Acta 64, 2295–2307.

Gunnarsson, I., Arnórsson, S., 2003. Silica scaling: the main obstacle in efficient use of high-temperature geothermal fluids. In: Proceedings International Geothermal Conference. Reykjavik. pp. 30–36.

Gunnarsson, I., Arnórsson, S., 2005. Impact of silica scaling on the efficiency of heat extraction from high-temperature geothermal fluids. Geothermics 34, 320–329.

Gunnarsson, I., Ívarsson, G., Sigfússon, B., Thrastarson, E.Ö., Gíslason, G., 2010. Reducing silica deposition potential in waste waters from Nesjavellir and Hellisheiði Power Plants, Iceland. In: Proceedings World Geothermal Congress. Bali.

Hair, M.L., Hertl, W., 1970. Acidity of surface hydroxyl groups. J. Phys. Chem. 74, 91–94.

Handley, K., Campbell, K., Mountain, B., Browne, P., 2005. Abiotic–biotic controls on the origin and development of spicular sinter: in situ growth experiments, Champagne Pool, Waiotapu, New Zealand. Geobiology 3, 93–114.

Harrar, J., Locke, F., Otto Jr, C., Lorensen, L., Monaco, S., Frey, W., 1982. Field tests of organic additives for scale control at the Salton Sea geothermal field. Soc. Pet. Eng. J. 22, 17–27.

Hawkins, C., Angheluta, L., Hammer, Ø., Jamtveit, B., 2013. Precipitation dendrites in channel flow. Europhys. Lett. 102, 54001.

Hawkins, C., Angheluta, L., Jamtveit, B., 2014. Hydrodynamic shadowing effect during precipitation of dendrites in channel flow. Phys. Rev. E 89, 022402.

Icopini, G.A., Brantley, S.L., Heaney, P.J., 2005. Kinetics of silica oligomerization and nanocolloid formation as a function of pH and ionic strength at 25 C. Geochim. Cosmochim. Acta 69, 293–303.

Iler, R.K., 1979. The Chemistry of Silica: Solubility, Polymerization, Colloid and Surface Pro Perties, and Biochemistry. Wiley, London.

Jones, B., Renaut, R.W., 2004. Water content of opal-A: implications for the origin of laminae in geyserite and sinter. J. Sediment. Res. 74, 117–128.

Jones, B., Renaut, R.W., 2010. Impact of seasonal changes on the formation and accumulation of soft siliceous sediments on the discharge apron of Geysir, Iceland. J. Sediment. Res. 80, 17–35.

Kitahara, S., 1960. The polymerization of silicic acid obtained by the hydrothermal treatment of quartz and the solubility of amorphous silica. Rev. Phys. Chem. Jpn. 30, 131–137.

Konhauser, K.O., Phoenix, V.R., Bottrell, S.H., Adams, D.G., Head, I.M., 2001. Microbial–silica interactions in Icelandic hot spring sinter: possible analogues for some Precambrian siliceous stromatolites. Sedimentology 48, 415–433.

Konhauser, K.O., Jones, B., Phoenix, V.R., Ferris, G., Renaut, R.W., 2004. The microbial role in hot spring silicification. AMBIO: J. Hum. Environ. 33, 552–558.

Meier, D., Gunnlaugsson, E., Gunnarsson, I., Jamtveit, B., Peacock, C., Benning, L., 2014. Microstructural and chemical variation in silica-rich precipitates at the Hellisheiði geothermal power plant. Mineral. Mag. 78, 1381–1389.

Morris, M. and Vossos, P.H. (1970) Large particle silica sols and method of production. Google Patents.

Mountain, B., Benning, L., Boerema, J., 2003. Experimental studies on New Zealand hot spring sinters: rates of growth and textural development. Can. J. Earth Sci. 40, 1643–1667.

Mroczek, E., McDowell, G., 1988. Silica scaling field experiments. In: New Zealand Geothermal Workshop. Auckland.

Mroczek, E., Graham, D., Bacon, L., 2011. Manila. Silica Deposition Experiments: Past Work and Future Research Directions Proceedings International Workshop on Mineral Scaling in Geothermal Environments.

Mroczek, E., Graham, D., Siega, C., Bacon, L., 2017. Silica scaling in cooled silica saturated geothermal water: comparison between Wairakei and Ohaaki geothermal fields, New Zealand. Geothermics 69, 145–152.

Noguera, C., Fritz, B., Clément, A., 2015. Precipitation mechanism of amorphous silica nanoparticles: a simulation approach. J. Colloid Interface Sci. 448, 553–563.

Okamoto, A., Saishu, H., Hirano, N., Tsuchiya, N., 2010. Mineralogical and textural variation of silica minerals in hydrothermal flow-through experiments: implications for quartz vein formation. Geochim. Cosmochim. Acta 74, 3692–3706.

Okazaki, T., Orii, T., Ueda, A., Ozawa, A., Kuramitz, H., 2017. Fiber optic sensor for Real-time sensing of silica scale formation in geothermal Water. Sci. Rep. 7.

Padilla, S.R.M., Barnett, P., Castro, M., Guerra, E., Henríquez, J.L., 2005. Silica polymerization and deposition trials at the Berlin geothermal Field, El Salvador. Proceedings World Geothermal Congress.

Parkhurst, D.L., Appelo, C., 2013. Description of Input and Examples for PHREEQC Version 3: a Computer Program for Speciation, Batch-Reaction, One-Dimensional Transport, and Inverse Geochemical Calculations. US Geological Survey.

Preston, L., Benedix, G., Genge, M., Sephton, M., 2008. A multidisciplinary study of silica sinter deposits with applications to silica identification and detection of fossil life on Mars. Icarus 198, 331–350.

Rimstidt, J.D., Barnes, H., 1980. The kinetics of silica-water reactions. Geochim. Cosmochim. Acta 44, 1683–1699.

Rimstidt, J., Cole, D., 1983. Geothermal mineralization. I. The mechanism of formation of the Beowawe, Nevada, Siliceous sinter deposit. Am. J. Sci. (United States) 283.

Rothbaum, H., Anderton, B., Harrison, R., Rohde, A., Slatter, A., 1979. Effect of silica polymerisation and pH on geothermal scaling. Geothermics 8, 1–20.

Seward, T., 1974. Determination of the first ionization constant of silicic acid from quartz solubility in borate buffer solutions to 350 C. Geochim. Cosmochim. Acta 38, 1651–1664.

Thórhallsson, S., Ragnars, K., Arnórsson, S., Kristmannsdóttir, H., 1975. Rapid scaling of silica in two district heating systems. In: United Nations Symposium on the Development and Use of Geothermal Resources. San Fransico. pp. 1445–1449.

Tobler, D.J., Benning, L.G., 2013. *In-situ* and time resolved nucleation and growth of silica nanoparticles forming under simulated geothermal conditions. Geochim. Cosmochim. Acta 114, 156–168.

Tobler, D.J., Stefansson, A., Benning, L.G., 2008. *In-situ* grown silica sinters in Icelandic geothermal areas. Geobiology 6, 481–502.

Tobler, D.J., Shaw, S., Benning, L.G., 2009. Quantification of initial steps of nucleation and growth of silica nanoparticles: an *in-situ* SAXS and DLS study. Geochim. Cosmochim. Acta 73, 5377–5393.

Tobler, D.J., Stawski, T.M., Benning, L.G., 2017. Silica and alumina nanophases: natural processes and industrial applications. New Perspectives on Mineral Nucleation and Growth. Springer, pp. 293–316.

Weres, O., Yee, A., Tsao, L., 1981. Kinetics of silica polymerization. J. Colloid Interface Sci. 84, 379–402.

Wirth, R., 2009. Focused Ion Beam (FIB) combined with SEM and TEM: advanced analytical tools for studies of chemical composition, microstructure and crystal structure in geomaterials on a nanometre scale. Chem. Geol. 261, 217–229.

Yokoyama, T., Sato, Y., Maeda, Y., Tarutani, T., Itoi, R., 1993. Siliceous deposits formed from geothermal water I. The major constituents and the existing states of iron and aluminium. Geochem. J. 27, 375–384.